On Lifetime Evaluation of Medium Voltage Drives Based on Modular Multilevel Converter

A. F. Cupertino, P. R. M. Junior, H. A. Pereira and G. A. Mendonça.

Published in:

IET Electric Power Applications

DOI (*link to publication from Publisher*):

10.1049/iet-epa.2018.5897

Publication year:

2019

Document Version:

Accepted author manuscript, peer reviewed version

Citation for published version:

A. F. Cupertino, P. R. M. Junior, H. A. Pereira and G.A. T.Mendonça, "On Life time Evaluation of Medium Voltage Drives Based on Modular Multilevel Converter," IET Electric Power Applications , vol. 13, no. 10, pp. 1453-1461, October 2019.
doi: 10.1049/iet-epa.2018.5897

IET Journals
The Institution of Engineering and Technology

On Lifetime Evaluation of Medium Voltage Drives Based on Modular Multilevel Converter

ISSN 1751-8644
doi: 0000000000
www.ietdl.org

Paulo R. M. Júnior[1], *Allan F. Cupertino*[2,3*], *Gabriel A. Mendonça*[3], *Heverton A. Pereira*[1]

[1] *Department of Electrical Engineering, Federal University de Viçosa, Viçosa, MG, Brazil*
[2] *Department of Materials Engineering, Federal Center for Technological Education of Minas Gerais,Belo Horizonte, MG, Brazil*
[3] *Graduate program in Electrical Engineering, Federal University of Minas Gerais, Belo Horizonte, MG, Brazil*
* *E-mail: afcupertino@ieee.org*

Abstract: Reliability is an important issue related to the modular multilevel converter (MMC) based medium voltage (MV) drives. The design for reliability (DFR) approach has been discussed in many power electronic systems in recent years. MMC based MV drives power losses and thermal cycling are strongly affected by start-up and low speed operation, since zero sequence current injection must be applied. In order to implement fast thermal simulations, the traditional DFR approach does not consider the heatsink thermal capacitance, which can significantly affect the MMC lifetime prediction. This paper discusses how the heatsink realizations (material, thickness) affect the MMC predicted lifetime and evaluates how the drive start-up time affects the damage in the power converter. The case study is based on a 1.4 MW slurry pump system driven by a three-phase induction motor. The lifetime evaluation of the MMC is realized through the Monte Carlo simulation. The results show that the traditional approach results in an underestimation of up to 42.5% of the converter lifetime. In addition, long start-up times lead to a longer lifetime when compared to the shorter start-up times, due to the reduced thermal stresses in the semiconductors.

1 Introduction

The Modular Multilevel Converter (MMC) is a topology with significant potential to be employed in electric drives [1]. The MMC concept has been proved in high voltage direct current (HVDC) systems and static synchronous compensator (STATCOMs) [2, 3]. Regarding application in electric drives, the MMC offers great advantages to other converters, such as: low harmonic content, which reduces thermal stress in the machine, low dv/dt, which reduces motor insulation stress, high efficiency and reduced common-mode voltage [4].

The Double-Star Chopper Cell (DSCC) is the most widespread MMC topology in the literature for variable speed electric drives [5]. However, this topology presents some limitations due to the high voltage oscillations of the submodule (SM) capacitors when the motor operates at low speed and high torque [1, 6, 7]. This restriction can be overcome by injecting a common-mode voltage and an alternating circulating current, where ripples at low-frequency can be shifted to others that are closer to the output rated frequency [6]. Nevertheless, this zero sequence injection increases the effective value of MMC arm currents during the motor start-up [8]. When this approach is considered, the MMC presents good performance for quadratic loads (e.g., pumps, blowers, compressors and fans), which are very common in industrial sectors such as mining, oil and gas, metal, paper, petrochemical and cement [5, 9, 10].

AC medium voltage converters play an important role in the industry and have high availability requirements, since a single failure may lead to a cost higher than the overall system costs. Therefore, the reliability is a very important variable in the converter design [27]. Technical surveys indicate that the lifetime target on electric drives can range from 5 to 20 years [12, 13]. Moreover, the power converter accounts until 65 % of the failures in this kind of system [14]. When compared to other topologies, the MMC has a larger number of components, such as semiconductor devices, which can increase the failure probability. Therefore, the design for reliability (DFR) approach is very important in this kind of converter.

In order to increase the system reliability, some methodologies have proven to be a potential solution, such as:

- Redundancy strategies [15, 16];
- Reliability-oriented design in order to correctly select the inverter components [17];
- Derating strategies [18–20];
- Optimization of the converter cooling system [21];
- Periodic preventive maintenance [22].

Several approaches to MMC lifetime evaluation are proposed in the literature, mainly focusing in HVDC systems. In [23], it is developed a simple thermal modeling method to estimate semiconductor junction temperature at periodic power loss profiles for the power devices in MMC HVDC systems. Additionally, reliability and redundancy configuration method of a hybrid MMC followed by the recommended redundant number of SMs for the design is proposed in [24]. In [25], it is compared the most employed lifetime models of semiconductors devices through an offshore wind farms based MMC. The impact of the thermal interface material thickness on the lifetime of the power modules for MMC HVDC applications is investigated in [26]. For the MMC based electric drive applications, the impact of various common-mode voltage and circulating current strategies on the power losses and thermal cycling of the semiconductor devices are evaluated in [8]. In [27], it is discussed a DFR applied to the rolling mills drive system, in which, in order to achieve the required reliability, proper evaluation and selection of power converter are conducted considering the thermal stress.

Nevertheless, some limitations are also identified in the literature. Firstly, in order to perform fast thermal simulations, the heatsink thermal capacitance is usually neglected. The heatsink thermal capacitance can affect considerably the thermal stresses during transients and the power cycling in the power devices. This is discussed in [28], which compares aluminum and copper heatsinks for a magnet supply system. Nevertheless, the technical literature does not discusses how the traditional lifetime evaluation affects the analysis, since it neglects the heatsink thermal capacitance. Thus, further investigation is needed to evaluate the effect of such approximation on the MMC topology lifetime analysis.

Moreover, the MMC based electric drives have a zero sequence injection which can change significantly the thermal cycling for low

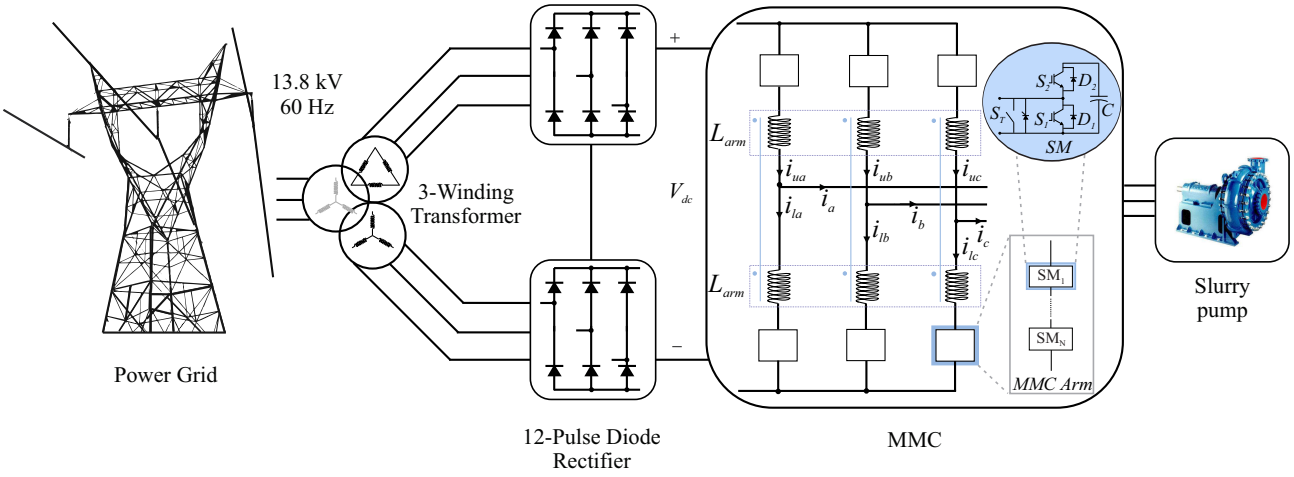

Fig. 1: MMC based slurry pump drive system

speed operation or during the start-up. Additionally, the start-up time affects the power cycling of the devices and can influence to some degree the converter reliability. Nevertheless, a quantitative analysis of the start-up time effect on the lifetime has not been presented in the technical literature.

Therefore, this work intends to fill these voids in the literature by providing the following contributions:

- Analysis of the thermal cycling impact on the converter lifetime during one year operation, considering start-up, steady-state and turn-off motor of the MMC based electric drive;
- Evaluation of the effect of different heatsink realizations on the lifetime evaluation procedure;
- Analysis of the motor start-up time on the MMC lifetime estimation.

The case study is based on a 1.4 MW slurry pump system driven by an induction motor. The remainder of this paper is organized as follows. In Section 2, the MMC drive topology and control strategies are presented. The methodology used to calculate the heatsink parameters is shown in Section 3. In Section 4, is presented the methodology used to calculate the MMC lifetime. The case study and the parameters of the system are presented in Section 5. Furthermore, the obtained results are shown and discussed in Section 6. Finally, the conclusions of this paper are stated in Section 7.

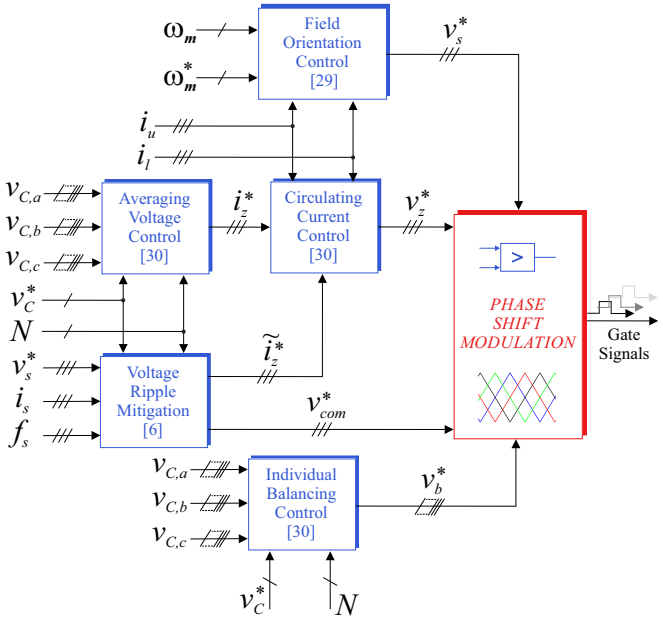

Fig. 2: Control scheme of the MMC based electric drive system

2 MMC Based Electrical Drive

The structure of the electrical drive system is shown in Fig. 1. As illustrated, the drive system is fed from the power supply through a 3-winding transformer and a 12-pulse uncontrolled rectifier. The slurry pump is driven at variable-speed by an induction motor supplied from the MMC. This paper is focused on the MMC analysis. The MMC topology used in this paper is the DSCC. In this topology, there are N SMs per arm, where each SM contains four semiconductor devices and one capacitor. The switch S_T, connected at the SM terminals, bypasses it in the occurrence of a failure. The arm inductance is represented by L_{arm}. Coupled inductors are generally used in MMC drive systems in order to reduce the volume and improve the MMC dynamics [6].

Regarding the control scheme, the strategy used is based on [6], which consists in the internal dynamics control, individual control and external dynamics control, as presented in Fig. 2 and detailed in Fig. 3. The internal control is based on a cascade control, in which the external loop is responsible for controlling the average SM capacitor voltages and manages the energy exchange in the converter. The internal loop is responsible for controlling the circulating current in order to mitigate the second order harmonic and improve converter stability. In order to reduce the oscillations in the capacitor voltages during low speeds, a strategy of voltage ripple mitigation (VRM) was used. This strategy consists of inserting an alternating circulating current and a common-mode voltage [6].

The individual control sets each SM at the reference voltage. In order to improve the individual balancing performance, a moving average filter (MAF) is used to attenuate the capacitor voltages ripple [30]. Finally, the external dynamics control is responsible for controlling the motor speed, which is based on the traditional rotor field orientation control (RFOC) [29]. The control signals are summed, normalized and compared by the voltage modulator. A Phase-Shifted PWM (PS-PWM) with third harmonic injection is considered in this work [30]. This strategy uses one carrier per SM. The voltage reference of each SM is compared with the carrier signal. If the voltage reference is higher than the carrier, the corresponding SM is inserted. Otherwise, if the voltage reference is lower than the carrier, the corresponding SM is bypassed. The switching frequency of each SM is equal to the carrier frequency. The carriers are phase shifted in order to generate the multilevel waveform at the converter output [30].

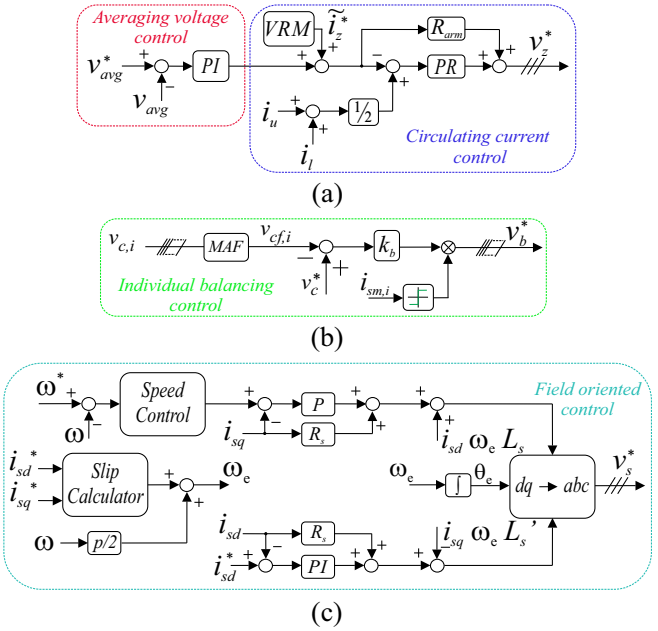

Fig. 3: Detailed control scheme of the system
(a) Internal dynamics control
(b) Individual control
(c) External dynamics control

3 Thermal model and Heatsink Design

As previously discussed, the reliability and lifetime of the converter are directly affected by the thermal cycling in the semiconductors [31]. The equivalent thermal circuit, Fig. 4, is employed to estimate the thermal response of the devices in each SM [32]. The case temperature, T_c, is estimated by a Cauer equivalent circuit whose power losses derive from the junction temperature, T_j. Alternatively, this junction temperature is estimated by a Foster equivalent circuit using the case temperature as reference [31]. The junction-to-case and case-to-heatsink thermal impedances are obtained from the semiconductor device datasheets. The power module used consists of a half-bridge 3300 V/200 A with part number FF200R33KF2C manufactured by Infineon. The thermal impedances of the power module are presented in Table 1. As observed, the junction to case thermal impedance (Z_{j-c}) is represented by a four layer foster model. The case to heatsink impedance (Z_{c-h}) is represented by a simple thermal resistance.

The detailed view of the power module and heatsink is presented in Fig. 5 (a). The heatsink parameters (thermal resistance and capacitance) are estimated based on [28], where a simplified heatsink model for power converter is proposed. This methodology considers a uniform temperature profile throughout the power devices baseplate and heatsink volume. The heatsink geometry has a simple rectangular cross-section and it is approximated by a simple orthogonal brick, as illustrated in Fig. 5 (b). In such conditions, the heatsink parameters can be computed by [28]:

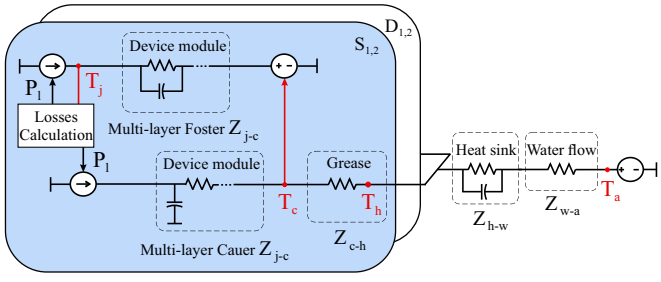

Fig. 4: Power semiconductor thermal model for a single MMC SM

Table 1 Power modules thermal impedance foster parameters [34]

Device	Parameter	$Z_{j-c,1}$	$Z_{j-c,2}$	$Z_{j-c,3}$	$Z_{j-c,4}$	Z_{c-h}
IGBT	$R_i(K/kW)$	25.65	14.25	3.42	13.68	49
	$\tau_i(s)$	0.03	0.1	0.3	1	-
Diode	$R_i(K/kW)$	48.6	27	6.48	25.92	93
	$\tau_i(s)$	0.03	0.1	0.3	1	-

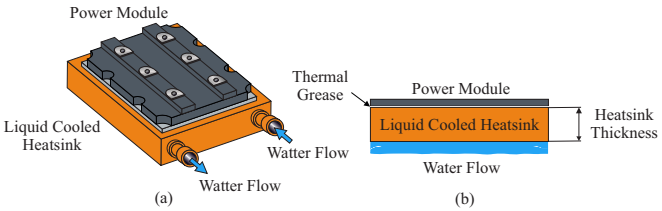

Fig. 5: Heatsink water cooling system
(a) Detailed view
(b) Simplified model

$$R_{h-w} = \frac{d_h}{\lambda_h A_h}, \tag{1}$$

$$C_{h-w} = c_h \rho_h d_h A_h, \tag{2}$$

where d_h is the heatsink thickness, λ_h is the thermal conductivity of the heatsink material, A_h is the heatsink surface area, c_h is the specific heat capacity and ρ_h is the material density. For comparison purposes, copper and aluminum heatsinks are used. Table 2 shows the parameters of these materials.

As a simplified approach, the heatsink area is considered to be equal to the total area of the power module, $A_h = 0.01022m^2$ from the device datasheet. As noted in (1) and (2), the values of R_{h-w} and C_{h-w} vary according to the thickness of the heatsink plate. In order to compare the MMC lifetime rates, heatsinks with two different thickness values are used, i.e., with 3 and 5 cm, since the semiconductor temperature depend on the heatsink dimensions and cooling system. The capacitance and resistance values of the heatsinks used in this work are presented in Table 3.

Finally, it is necessary to calculate the thermal resistance representing the water cooling system, R_{w-a}, in order to improve the heat exchange from the heatsink to the ambient. This resistance can be calculated by:

$$R_{w-a} = \frac{1}{h_c A_h}, \tag{3}$$

where h_c is the water flow convection coefficient. According to [33], the variable h_c can range from 50 to 2500 $W/(m^2K)$, depending

Table 2 Copper and aluminum properties

Parameters	Aluminum	Copper
Thermal conductivity $W/(m\,^\circ\mathrm{C})$	238	400
Specific heat capacity $J/(kg\,^\circ\mathrm{C})$	900	385
Density kg/m^3	2700	8960

Table 3 Heatsink equivalent thermal circuit parameters

Parameter	Aluminum 5 cm	Aluminum 3 cm	Copper 5 cm	Copper 3 cm
R_{h-w} $^\circ\mathrm{C}/W$	0.02	0.012	0.012	0.00732
C_{h-w} $J/^\circ\mathrm{C}$	1241	745	1057	1762

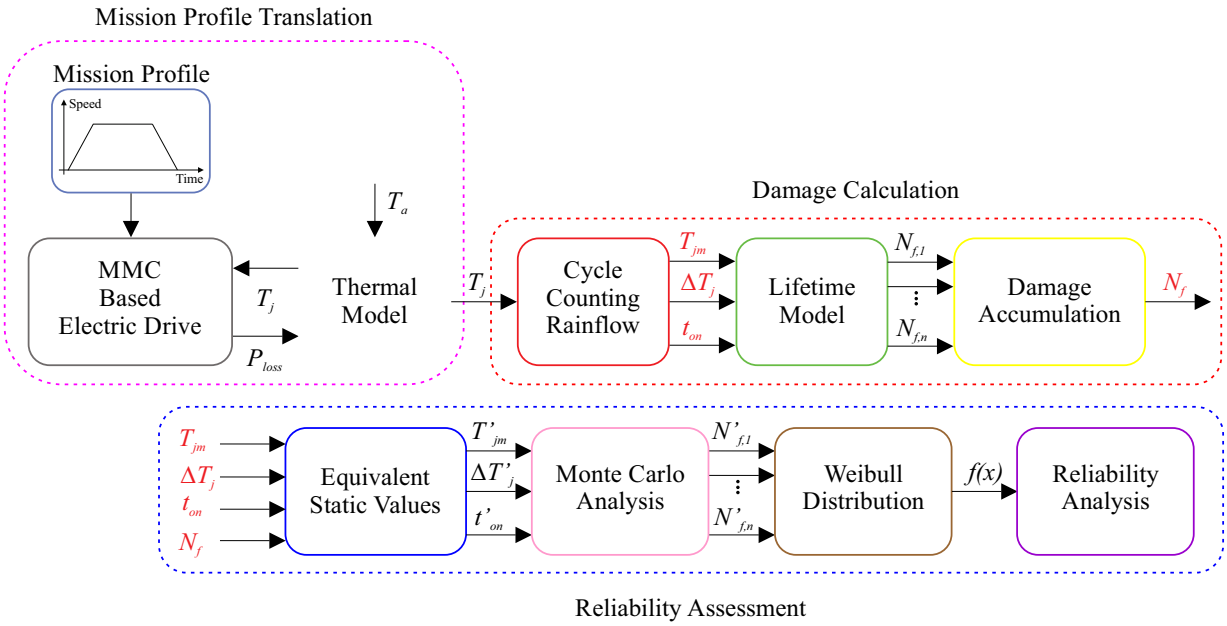

Fig. 6: Lifetime evaluation flowchart

on the speed and type of water flow, temperature dependent properties and pressure. The necessary value is determined through thermal simulations, which are carried out in order to maintain the junction and case temperatures within the limits for the worst conditions (for the selected power modules, 120 °C in the junction and 80 °C in the device case). Therefore, $h_c = 1250\ W/(m^2K)$ is employed, which is a reasonable value according to [33]. Regarding to the heat transfer fluid, water glycol solution is employed since, according to [35], it can be used for both copper and aluminum heatsinks.

The parameters computed by equations (1) and (2) are a rough estimation of the heatsink parameters. Furthermore, the proposed methodology of lifetime estimation can be applied if the heatsink parameters are known. A detailed modeling of heatsinks considering the shape, flow characteristics and cooling liquid parameters usually involves complex heat transfer models which are solved in Finite Element Method (FEM) packages. Based on these models, the thermal parameters (thermal resistance and capacitance) can be obtained and used by the thermal simulation and lifetime estimation flowchart. Nevertheless, the analysis of complex heatsink shapes is out the scope of this work.

4 Lifetime Evaluation

The damage in the semiconductor devices is related to thermal cycling, which causes thermal fatigue in the solders and bond-wires. According to [12], there are three dominant wear-out mechanisms on IGBT due to thermal stress: the bond-wire liftoff, chip solder joint cracking and base plate solder joint cracking.

In this paper, the lifetime evaluation is focused on the semiconductor devices, where the bond-wire failures are analyzed due to the thermal cycling. Thus, it is necessary to estimate the junction temperature, T_j, of the semiconductors according to the mission profile, as discussed in Section 3. The lifetime evaluation is performed by the mission profile translation, damage calculation and reliability assessment. The complete flowchart used in this paper is shown in Fig. 6.

4.1 Mission Profile Translation to Thermal Loading

The mission profile for electric drive systems is the motor speed reference, since the current flowing in the converter is related to the torque and speed profiles. The mission profile needs to be translated into the thermal loading of the semiconductor [12]. Basically, the power losses, P_{loss}, of the devices are obtained through a Look-Up Table (LUT) relating the conduction and switching losses of the IGBTs and diodes, which are provided by datasheets of the devices. The junction temperature, T_j, can be estimated from the thermal model as presented in Fig. 4.

Since the load follows a quadratic speed torque curve, only the speed mission profile is employed in this work. However, the presented methodology can be easily extended, where measurements of the motor speed and current profiles are applied.

4.2 Damage Calculation

The junction temperature obtained in the previous step is an irregular time-varying signal due to two thermal cycling: a low and a high frequency cycling. The first is associated with the variation of the motor speed and torque reference, from the mission profile. The latter is related to the current frequency of the devices, which depends on the injected zero sequence voltage and output currents. The rainflow counting algorithm is used in order to obtain regular thermal cycles and decouple the parameters that affect the degradation of the devices [32], namely, the mean junction temperature, T_{jm}, cycle amplitude, ΔT_j and the heating time during the cycling period, t_{on}. Then, these parameters can be directly applied to the lifetime model from which the number of cycles to failure can be computed.

The lifetime model employed in this work is given by [36]:

$$N_f = A\Delta T_j^{\beta_1} exp\left(\frac{\beta_2}{T_{jm}+273}\right) t_{on}^{\beta_3} I^{\beta_4} V^{\beta_5} D^{\beta_6}. \quad (4)$$

The parameters of this lifetime model are obtained from [36] through the curve fitting of accelerating test results. These parameters are presented in Table 4.

The number of failures, N_f, is calculated for three motor operating regions, that present different thermal behavior. The first region is the motor start-up, $N_{f,1}$, where the zero-sequence is used to mitigate the ripple of the capacitors at low speeds. The second is the steady-state, $N_{f,2}$, when the motor is operating at rated speed, and it is not necessary to use zero-sequence injection. Finally, the third is the motor braking, $N_{f,3}$, where the zero-sequence injection is also used as in the first region to maintain the SM capacitors controlled in the turn-off process.

This approach is performed for each semiconductor of the SM ($S1$, $S2$, $D1$ and $D2$). Then, the lifetime consumption (LC) is calculated considering a duty cycle of 8 hours per day for one year. The

Table 4 Parameters for the calculation of N_f based on the Bayerer Model [37]

Parameter	Symbol	Limits	Coef.	Value
Tech. factor	A	-	-	9.3410^{14}
Temp. fluctuation	ΔT_j	45-150 °C	β_1	-4.416
Min. junction temp.	$T_{j,min}$	20-120 °C	β_2	1285
Cyc. period	t_{on}	1-60s	β_3	-0.463
Current bond foot	I	3-23A	β_4	-0.716
Block. voltage	V	6-33V	β_5	-0.761
Bond-wire diameter	D	75-500μm	β_6	-0.5

LC indicates how much life of the device has been damaged during the operation. When the LC value reaches to unity (100 %), this indicates that the analyzed device has reached the end of life. Fig. 7 shows the mission profile and division of the lifetime calculation into three regions. The lifetime consumption per region is calculated by:

$$L_{C(1,2,3)} = \sum_k \frac{1}{N_{f,(1,2,3)_k}}, \tag{5}$$

and the total lifetime consumption is given by:

$$L_{C,t} = L_{C,1} + L_{C,2} + L_{C,3}. \tag{6}$$

4.3 *Reliability Assessment*

In the previous section, a fixed value of the lifetime consumption is obtained considering that all the power semiconductors will fail at the same time. However, depending of the fabrication process and power loading, the electrical parameters of the semiconductor devices may have some variations [37]. Thus, a statistical analysis based on the Monte-Carlo simulation is performed for computing the lifetime distribution and the reliability metrics.

Firstly, the parameters of ΔT_j, T_{jm} and t_{on} must be converted into equivalent static values $\Delta T_j'$, T_{jm}' and t_{on}', which results in the same lifetime when the static values on the lifetime model are applied [38]. With the equivalent static values, a variation of 5% is performed in these parameters and those presented in Table 4. In addition, the Monte-Carlo analysis is simulated using 10,000 samples, from which the Weibull probability distribution function (Weibull-PDF), $f(x)$, of the power device can be constructed.

The unreliability of the power device can be evaluated by considering the cumulative density function (CDF), F(x), which is the integral of PDF. From the CDF, also referred to as unreliability function, it is possible to define a point in time (in years) when the accumulated failure rate reached x%, B_x [38]. Finally, in order to further obtain a system-level reliability assessment based on the component-level, it is necessary to calculate the unreliability function for each MMC SM, as follows:

$$F_{SM}(x) = 1 - \prod_{i=1}^{4}(1 - F_i(x)), \tag{7}$$

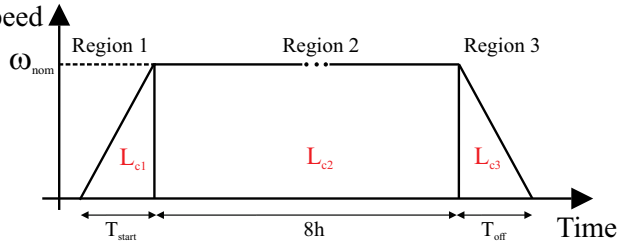

Fig. 7: Daily profile and damage separation into regions

where $F_i(x)$ is the unreliability of each device and i = 1, 2, 3 and 4 for S_1, S_2, D_1 and D_2, respectively. Then, the system-level unreliability can be computed by:

$$F_{MMC}(x) = 1 - \prod_{i=1}^{6N}(1 - F_{SM,i}(x)). \tag{8}$$

Once the total unreliability function of the MMC system is found, F_{MMC}, the same approach of component-level can be evaluated in order to calculate the B_x of the MMC.

It is important to mention that the methodology of lifetime evaluation presented in this work can be adapted to other multilevel converters topologies and applications. Nevertheless, this is out of the scope of the present work.

5 Case Study

The main circuit parameters of the MMC based electric drive considered in this paper are presented in Table 5. The parameters of the induction high power motor that drives the slurry pump are shown in Table 6. The mission profile cycle is defined on a daily basis, as depicted in Fig. 7, and is used for evaluation throughout the course of one year. In this analysis, the ambient temperature is considered constant and equal to 40 °C.

The case study of this paper compares the lifetime of the MMC with aluminum and copper heatsinks of 3 and 5 cm thickness. Firstly, a comparison of the system level reliability is evaluated based on the different heatsink realizations presented in Table 3 for the same speed mission profile, where the motor is accelerated to its rated speed in 10 seconds. The traditional approach (thermal simulations without considering the heatsink thermal capacitance) is benchmarked with the lifetime analysis considering the heatsink parameters. Finally, the start-up time ranges from 5 to 90 seconds

Table 5 MMC specifications

Parameter	Value
Rated apparent power (S)	2 MVA
Pole to pole dc voltage (V_{dc})	12 kV
Arm inductance (L_{arm})	7.7 mH
Arm resistance (R_{arm})	0.065 Ω
SM capacitance (C)	2 mF
Nominal SM voltage ($v_{sm,n}$)	1.71 kV
Switching frequency (f_s)	945 Hz
Number of SMs (N)	7 per arm

Table 6 Parameters of the induction motor

Parameter	Value
Rated active power (P)	1.4 MW
Rated rms line-to-line voltage (v_m)	7.2 kV
Rated line current (i_s)	134 A
Rated frequency (f)	60 Hz
Rated rotational speed (n_m)	1792 rpm
Rated power factor	0.87
Rated efficiency (η)	96.7 %
Number of poles (p)	4
Rated torque (T_{nom})	7.46 kNm
Rotor resistance (R_r)	0.15386 Ω
Stator resistance (R_s)	0.13735 Ω
Magnetizing inductance (L_m)	217.3 mH
Stator leakage inductance (L_{ls})	7.34 mH
Rotor leakage inductance (L_{lr})	7.34 mH
Total inertia ($J_{motor} + J_{pump}$)	59 kgm^2

in order to evaluate its impact on the MMC unreliability. Simulations are performed in PLECS environment and MATLAB, aiming to compare the MMC B_{10} lifetime for all cases.

6 Results and Discussion

6.1 MMC based electric drive performance

The start-up dynamics of the system is illustrated in Fig. 8. The speed control can be analyzed in Fig. 8 (a), the motor speed profile adopted is a ramp-up time of 10 seconds with constant acceleration, and steady-state motor speed set to 1800 rpm. The speed error is lower than 0.5 %. Fig. 8 (b) illustrates the motor stator currents. At t = 0.1 s, the magnetizing current is inserted and, at t = 2 s, the motor begins to accelerate. The VRM is inserted up to 5.5 seconds, where the motor has already reached 30 % of rated speed. In steady-state the peak of the motor currents is 196 A. The multilevel line-to-line stator voltages is shown in Fig. 8 (c). Finally, the capacitor voltages of the upper arm are shown in Fig. 8 (d). The capacitor voltage ripples do not exceed the 5 % range during the start-up.

6.2 Lifetime Analysis for Different Heatsinks

The thermal stress of the MMC was evaluated before the lifetime evaluation of the semiconductors devices for the different heatsink designs presented in Table 3. Fig. 9 shows the junction temperature of the most stressed case, 5 cm aluminum heatsink neglecting its thermal capacitance.

For the start-up region, as illustrated in Fig. 9 (a), the machine was first magnetized and, after 2 seconds, the speed mission profile was applied. At this moment, the zero sequence was inserted to mitigate the SMs capacitors ripple. Applied only at low speeds, the zero sequence was injected until the motor reached 30 % of the rated speed, at 5.3 seconds. It is possible to observe an irregular thermal cycling that can lead to a significant damage in the semiconductors.

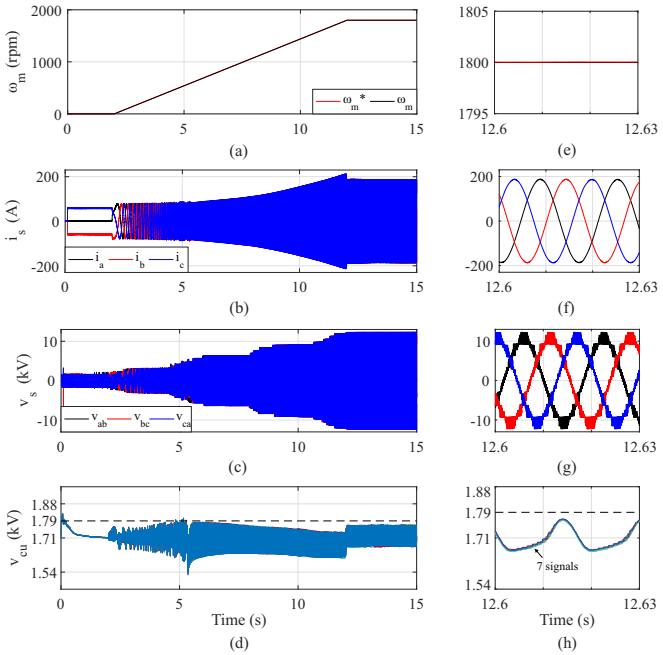

Fig. 8: Start-up of the MMC based electric drive system
(a) Speed control
(b) Stator currents
(c) Stator voltages
(d) Capacitors voltages of the upper arm
(e) Detail of speed control
(f) Detail of stator currents
(e) Detail of stator voltages
(f) Detail of capacitors voltages of the upper arm

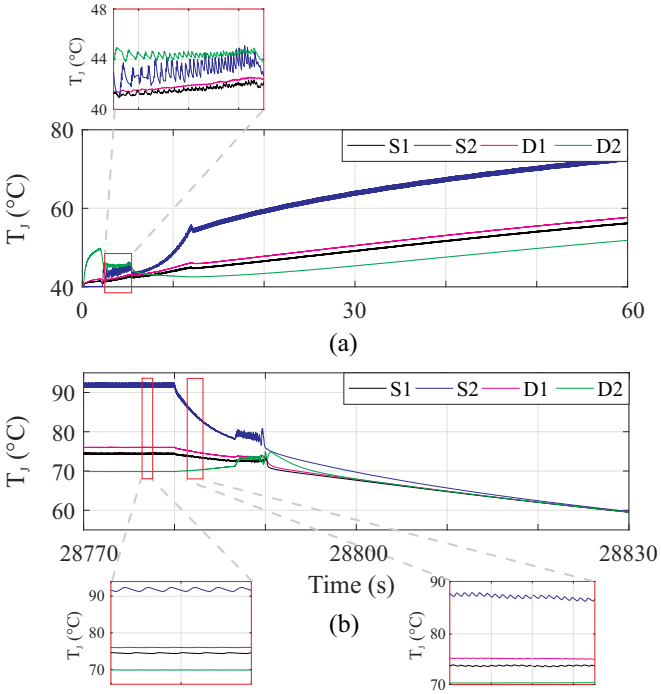

Fig. 9: Junction temperature of 5 cm aluminum heatsink neglecting its thermal capacitance
(a) Start-up region
(b) Steady-state and braking regions

Fig. 9 (b) illustrates the steady-state and the braking motor regions. At steady-state, it is possible to notice a well-defined thermal cycle, reaching an oscillation of 1 °C for the most stressed device, S_2. In the braking region, it is noticeable the temperature dropping and, as the motor reaches low speed operating conditions, the zero sequence is inserted again.

After the estimation of the junction temperature, the thermal cycles were counted based on the rainflow algorithm. The number of cycles obtained from the lifetime model was accumulated, allowing the calculation of the life consumption, $L_{C,t}$, of the semiconductor devices. Fig. 10 shows the lifetime consumption of the most stressed device for all heatsink realizations, namely S_2. As observed, Regions 1 and 3 have the highest lifetime consumption, due to the mission profile cycling and the zero sequence at low speeds. Region 2 presents the lowest lifetime consumption due to the low temperature fluctuations, ΔT_j, of the devices around a constant average temperature, T_{jm}.

The thermal capacitance of the heatsink directly affects the lifetime consumption of the semiconductors. For Region 1, the thermal capacitance increases the time constant of the thermal system, thus reducing the lifetime consumption compared to the same heatsink without the thermal capacitance. For Region 3, the opposite is observed, as a system with lower thermal capacitance becomes an attractive solution. The difference in lifetime consumption between

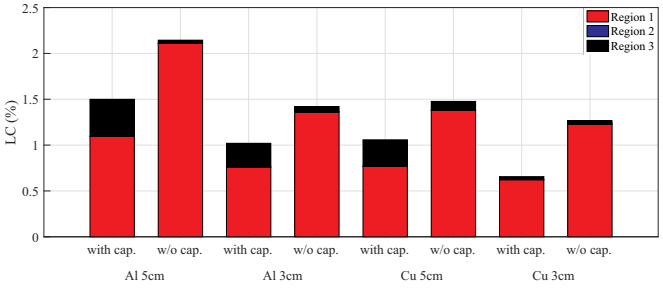

Fig. 10: Life consumption (LC) per year of the most stressed device (S_2)

the presented cases is due to the parameters of the heatsink equivalent thermal circuit, since these parameters depend both on its thickness and material. Thinner heatsinks lead to a lower thermal resistance, which results in a lower temperature in steady-state and consequently a decrease in the LC.

A reliability assessment of the MMC was carried out through the Monte Carlo analysis to obtain the B_{10} lifetime and compare the impact of the thermal capacitance. The system level unreliability function considering 5 cm heatsinks are presented in Fig. 11. As observed for the aluminum heatsink, the MMC B_{10} for the case without and with capacitance are 9.6 and 13.8 years, respectively. For the copper heatsink, the MMC B_{10} is 13.8 years without the thermal capacitance and 24 years, considering the thermal capacitance. The consideration of the thermal capacitance led to a 30.44% increase in the lifetime of aluminum and 42.5% for the copper sink. Therefore, the traditional approach (which neglects the effect of heatsink thermal capacitance) significantly underestimates the converter lifetime.

After significant impact of the thermal capacitance on the MMC lifetime was verified, a study was carried out to compare the lifetime for different thicknesses of heatsinks, all considering the thermal capacitance. The result is shown in Fig. 12.

As observed for the aluminum heatsink, the MMC B_{10} lifetime are 13.8 and 24 years for the 5 and 3 cm, respectively. On the other hand, the copper heatsink obtained a 24-year duration for the 5 cm heatsink and 37.6 years for the 3 cm heatsink. An increase of 73.91% is observed when using the 3 cm aluminum heatsink compared to 5 cm. This increase is 56.67% for copper. This increased lifetime is due to the variation of the heatsink equivalent circuit parameters, since a thinner heatsink has a lower resistance, reducing the semiconductors temperature in steady-state. The thermal capacitance is also reduced for the thinner heatsink, which decreases the damage on the braking region.

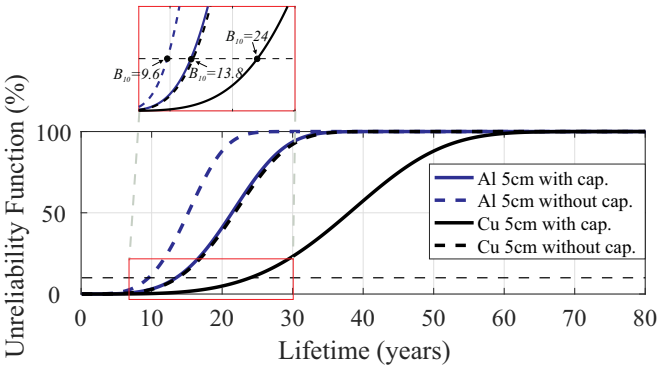

Fig. 11: Effect of the heatsink capacitance in the MMC unreliability function (thickness = 5 cm)

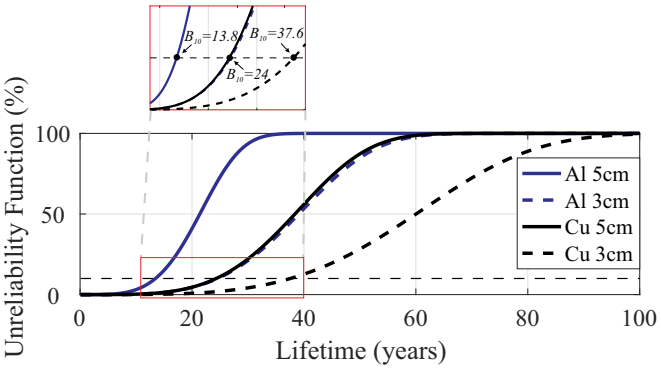

Fig. 12: Effect of the heatsink thickness in the MMC unreliability function considering the thermal capacitance

6.3 Analysis of the impact of the motor start-up time on the MMC lifetime

Furthermore, the effect of the motor start-up time in the B_{10} lifetime was evaluated. The case with the longest MMC B_{10} lifetime (3 cm copper heatsink) was selected. The motor start-up time ranged from 5 to 90 seconds. As shown in Fig. 13, MMC has a shorter lifetime for low start-up times. As the start-up time increases, the lifetime also increases. This fact can be justified by the analysis of arm currents, as shown in Fig .14, which directly affects the current flowing in the semiconductor devices.

As observed in Fig. 14(a), for a start-up time of 5 seconds, the arm currents during the zero sequence injection reaches 180 A. At the end of the motor acceleration, a maximum current of 175 A and a steady state peak current of 135 A were observed. These current values above the nominal current significantly increase the life consumption of semiconductor devices, which allows for a MMC lifetime B_{10} of 32 years for this occasion.

Fig. 14 (b) illustrates the arm currents for a start-up time of 30 seconds. At this time, the peak zero sequence current injection was

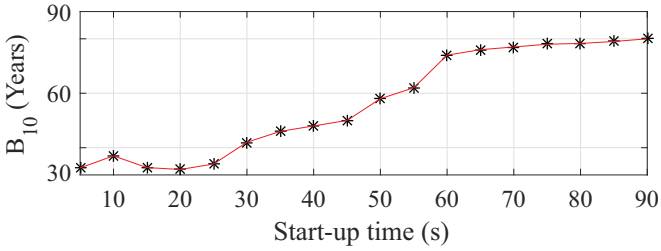

Fig. 13: Impact of the start-up time on the MMC B_{10} lifetime

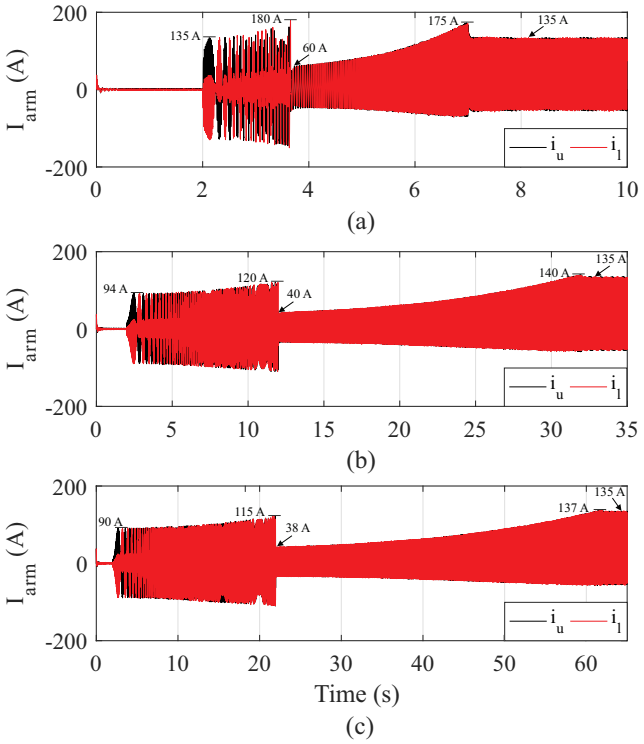

Fig. 14: Impact of the start-up time on the converter arm currents
(a) 5-second start-up
(b) 30-second start-up
(c) 60-second start-up

reduced to 120 A, while the peak at the end of the acceleration was 140 A. When the time of the start-up increases, it was possible to reduce these current peaks, increasing the B_{10} up to approximately 44 years.

Finally, Fig. 14 (c) shows the arm currents for the start-up time of 60 seconds. For this case, the peaks of the arm currents during zero sequence injection and at the end of the acceleration were 115 A and 137 A, respectively, while the B_{10} lifetime was 70 years. For start-up times longer than 60 seconds, it is noted that the lifetime of the converter does not increase significantly. This happens because, after a certain point, the increased start-up time does not reduce significantly the arm currents during the zero sequence injection.

7 Conclusions

This work presented the lifetime evaluation procedure of a MMC based MV drive. The physics of failure models are employed to estimate the lifetime of the power converter for an operation mission profile. Different heatsink realizations are compared.

As observed, the heatsink thermal capacitance has a significant impact on the unreliability curves of the power converter and consequently on the predicted lifetime. If such thermal capacitance is not considered, the converter lifetime can be underestimated up to 30 % for the aluminum and 40 % for the copper heatsink. As for the heatsink material composition, the copper heatsinks present a better performance in terms of damage on power semiconductors, in which the lifetime of the MMC based MV drive using the 5 cm copper heatsink with thermal capacitance can be increased up to 70 % when compared to aluminum under the same conditions. Nevertheless, this solution is more expensive and some optimization can be considered for the selection of the best solution in order to reduce the life cycle cost.

Finally, regarding the start-up time, small values can result in high currents in the power switches, which increases the power cycling and the damage to the power switches. Long start-up times result in reduced thermal stresses and are more interesting from the reliability point of view. By increasing the start-up time from 10 seconds to 1 minute, the lifetime of the converter power devices can be increased up to two times.

8 Acknowledgment

This study was financed in part by the Coordenação de Aperfeiçoamento de Pessoal de Nível Superior - Brasil (CAPES) - Finance Code 001, Conselho Nacional de Desenvolvimento Científico e Tecnológico (CNPq) and Fundação de Amparo à Pesquisa do Estado de Minas Gerais (FAPEMIG).

9 References

1 Y. S. Kumar and G. Poddar, "Control of medium-voltage ac motor drive for wide speed range using modular multilevel converter," *IEEE Trans. on Ind. Electronics*, vol. 64, no. 4, pp. 2742–2749, April 2017.

2 M. Saeedifard and R. Iravani, "Dynamic performance of a modular multilevel back-to-back hvdc system," *IEEE Trans. on Power Delivery*, vol. 25, no. 4, pp. 2903–2912, Oct 2010.

3 H. M. P. and M. T. Bina, "A transformerless medium-voltage statcom topology based on extended modular multilevel converters," *IEEE Trans. on Power Electronics*, vol. 26, no. 5, pp. 1534–1545, May 2011.

4 A. Antonopoulos, L. Ängquist, S. Norrga, K. Ilves, L. Harnefors, and H. Nee, "Modular multilevel converter ac motor drives with constant torque from zero to nominal speed," *IEEE Trans. on Ind. Appl.*, vol. 50, no. 3, pp. 1982–1993, May 2014.

5 H. Akagi, "Multilevel converters: Fundamental circuits and systems," *Proceedings of the IEEE*, vol. 105, no. 11, pp. 2048–2065, Nov 2017.

6 M. Hagiwara, I. Hasegawa, and H. Akagi, "Start-up and low-speed operation of an electric motor driven by a modular multilevel cascade inverter," *IEEE Transactions on Ind. Applications*, vol. 49, no. 4, pp. 1556–1565, July 2013.

7 B. Li, S. Zhou, D. Xu, S. J. Finney, and B. W. Williams, "A hybrid modular multilevel converter for medium-voltage variable-speed motor drives," *IEEE Trans. on Power Electronics*, vol. 32, no. 6, pp. 4619–4630, June 2017.

8 X. Han, Q. Yang, L. Wu, and M. Saeedifard, "Analysis of thermal cycling stress on semiconductor devices of the modular multilevel converter for drive applications," in *IEEE Applied Power Electronics Conference and Exposition*, March 2016, pp. 2957–2962.

9 A. Dekka, B. Wu, R. L. Fuentes, M. Perez, and N. R. Zargari, "Evolution of topologies, modeling, control schemes, and applications of modular multilevel converters," *IEEE Journal of Emerging and Selected Topics in Power Electronics*, vol. 5, no. 4, pp. 1631–1656, Dec 2017.

10 S. Kouro, J. Rodriguez, B. Wu, S. Bernet, and M. Perez, "Powering the future of industry: High-power adjustable speed drive topologies," *IEEE Ind. Applications Magazine*, vol. 18, no. 4, pp. 26–39, July 2012.

11 P. P. O'Connor and A. Kleyner, *Practical Reliability Engineering*, 5th ed. Wiley Publishing, 2012.

12 H. Wang, M. Liserre, F. Blaabjerg, P. de Place Rimmen, J. B. Jacobsen, T. Kvisgaard, and J. Landkildehus, "Transitioning to physics-of-failure as a reliability driver in power electronics," *IEEE Journal of Emerging and Selected Topics in Power Electronics*, vol. 2, no. 1, pp. 97–114, March 2014.

13 J. Falck, C. Felgemacher, A. Rojko, M. Liserre, and P. Zacharias, "Reliability of power electronic systems: An industry perspective," *IEEE Industrial Electronics Magazine*, vol. 12, no. 2, pp. 24–35, June 2018.

14 K. J. P. Macken, I. T. Wallace, and M. H. J. Bollen, "Reliability assessment of motor drives," in *2006 37th IEEE Power Electronics Specialists Conference*, June 2006, pp. 1–7.

15 J. V. M. Farias, A. F. Cupertino, H. A. Pereira, S. I. S. Junior, and R. Teodorescu, "On the redundancy strategies of modular multilevel converters," *IEEE Trans. on Power Delivery*, vol. 33, no. 2, pp. 851–860, April 2018.

16 P. Tu, S. Yang, and P. Wang, "Reliability and cost based redundancy design for modular multilevel converter," *IEEE Trans. on Ind. Electronics*, pp. 1–1, 2018.

17 Y. Yang, A. Sangwongwanich, and F. Blaabjerg, "Design for reliability of power electronics for grid-connected photovoltaic systems," *CPSS Trans. on Power Electronics and Applications*, vol. 1, no. 1, pp. 92–103, Dec 2016.

18 I. Vernica, K. Ma, and F. Blaabjerg, "Optimal derating strategy of power electronics converter for maximum wind energy production with lifetime information of power devices," *IEEE Journal of Emerging and Selected Topics in Power Electronics*, vol. 6, no. 1, pp. 267–276, March 2018.

19 H. M. N. Achiri, V. Smidl, and Z. Peroutka, "Mitigation of electric drivetrain oscillation resulting from abrupt current derating at low coolant flow rate," in *IECON 2015 - IEEE Industrial Electronics Society*, Nov 2015, pp. 003 638–003 642.

20 L. Maharjan, T. Yamagishi, H. Akagi, and J. Asakura, "Fault-tolerant operation of a battery-energy-storage system based on a multilevel cascade pwm converter with star configuration," *IEEE Transac. on Power Electronics*, vol. 25, no. 9, pp. 2386–2396, Sep. 2010.

21 D. Christen, M. Stojadinovic, and J. Biela, "Energy efficient heat sink design: Natural versus forced convection cooling," *IEEE Trans. on Power Electronics*, vol. 32, no. 11, pp. 8693–8704, Nov 2017.

22 H. Wang, K. Ma, and F. Blaabjerg, "Design for reliability of power electronic systems," in *IECON - IEEE Industrial Electronics Society*, Oct 2012, pp. 33–44.

23 Y. Zhang, H. Wang, Z. Wang, Y. Yang, and F. Blaabjerg, "Simplified thermal modeling for igbt modules with periodic power loss profiles in modular multilevel converters," *IEEE Trans. on Ind. Electronics*, pp. 1–1, 2018.

24 J. Xu, P. Zhao, and C. Zhao, "Reliability analysis and redundancy configuration of mmc with hybrid submodule topologies," *IEEE Trans. on Power Electronics*, vol. 31, no. 4, pp. 2720–2729, April 2016.

25 Y. Zhang, H. Wang, Z. Wang, Y. Yang, and F. Blaabjerg, "Impact of lifetime model selections on the reliability prediction of igbt modules in modular multilevel converters," in *IEEE Energy Conversion Congress and Exposition*, Oct 2017, pp. 4202–4207.

26 Y. Zhang, H. Wang, Z. Wang, Y. Yang and F. Blaabjerg, "Impact of the thermal-interface-material thickness on igbt module reliability in the modular multilevel converter," in *2018 International Power Electronics Conference*, May 2018, pp. 2743–2749.

27 V. de Nazareth Ferreira, A. F. Cupertino, H. A. Pereira, A. V. Rocha, S. I. Seleme, and B. de Jesus Cardoso Filho, "Design and selection of high reliability converters for mission critical industrial applications: A rolling mill case study," *IEEE Trans. on Ind. Applications*, vol. 54, no. 5, pp. 4938–4947, Sept 2018.

28 P. Asimakopoulos, K. Papastergiou, T. Thiringer, and M. Bongiorno, "Heat sink design considerations in medium power electronic applications with long power cycles," in *European Conference on Power Electronics and Applications*, Sept 2015, pp. 1–9.

29 D. W. Novotny and T. Lipo, *Vector Control and Dynamics of AC Drives*. Clarendon Press, 1996.

30 M. Hagiwara and H. Akagi, "Control and experiment of pulsewidth-modulated modular multilevel converters," *IEEE Trans. on Power Electronics*, vol. 24, no. 7, pp. 1737–1746, July 2009.

31 Q. Tu and Z. Xu, "Power losses evaluation for modular multilevel converter with junction temperature feedback," in *2011 IEEE Power and Energy Society General Meeting*, July 2011, pp. 1–7.

32 K. Ma, M. Liserre, F. Blaabjerg, and T. Kerekes, "Thermal loading and lifetime estimation for power device considering mission profiles in wind power converter," *IEEE Trans. on Power Electronics*, vol. 30, no. 2, pp. 590–602, Feb 2015.

33 F. P. Incropera and D. P. DeWitt, *Fundamentals of Heat and Mass Transfer*, 4th ed. New York City, New York: John Wiley and Sons, Inc., 1996.

34 IGBT-module FF200R33KF2C, Infineon Technologies.

35 'Lytron applications notes', https://www.lytron.com/Tools-and-Technical-Reference/Application-Notes, acessed 01 February 2019.

36 R. Bayerer, T. Herrmann, T. Licht, J. Lutz, and M. Feller, "Model for power cycling lifetime of igbt modules - various factors influencing lifetime," in *International Conference on Integrated Power Electronics Systems*, March 2008, pp. 1–6.

37 P. D. Reigosa, "TSmart Derating of Switching Devices for Designing More Reliable PV Inverters," Master's thesis, Aalborg University, Denmark, 2014.

38 A. Sangwongwanich, Y. Yang, D. Sera, and F. Blaabjerg, "Lifetime evaluation of grid-connected pv inverters considering panel degradation rates and installation sites," *IEEE Trans. on Power Electronics*, vol. 33, no. 2, pp. 1225–1236, Feb 2018.